Hydroxypropyl-β-cyclodextrin/thymoquinone inclusion complex inhibits non-small cell lung cancer progression through NF-κB-mediated ferroptosis

WEI-WEI ZHENG[1], JIA-XUAN DING[2], YANG-XIN LIANG[2] and LING YE[2]

[1]Department of Radiation Oncology, Ma'anshan People's Hospital, Ma'anshan, Anhui 243000, P.R. China;
[2]Department of Radiation Oncology, Sun Yat-sen Memorial Hospital, Sun Yat-sen University, Guangzhou, Guangdong 510120, P.R. China

Received May 3, 2025; Accepted August 22, 2025

DOI: 10.3892/or.2025.8990

Abstract. Thymoquinone (TQ) is a quinone isolated from the black seed *Nigella sativa* and has been extensively investigated in the pharmaceutical field due to its promising therapeutic value. There have been reports on the potential anti-cancer properties of TQ, whereas the clinical application of TQ is greatly restricted by its low water solubility and poor delivery. In the present study, TQ was encapsulated into hydroxypropyl-β-cyclodextrin (HP-β-CD) using the freeze-drying method to form a TQ/HP-β-CD inclusion complex. Then, the TQ/HP-β-CD inclusion complex was characterized by Fourier transform infrared, differential scanning calorimetry, X-ray diffraction and scanning electron microscopy. HP-β-CD as an excipient significantly enhances the water solubility of TQ, and TQ/HP-β-CD demonstrated excellent biocompatibility on normal cells both *in vitro* and *in vivo*. Moreover, the complexation with HP-β-CD enhanced the anticancer activity of TQ against non-small cell lung cancer cells and its mechanism of action is related to ferroptosis mediated by NF-κB. Such an enhanced cytotoxic effect may be attributed to the effective complexation of TQ in HP-β-CD, which enhances its water solubility and bioavailability.

Introduction

As the most common cause of cancer-related deaths in the world, lung cancer causes ~1.8 million deaths every year (1), of which non-small-cell lung cancer (NSCLC) accounts for ~80% of lung cancer cases and its incidence rate is increasing yearly (2). Early diagnosis of lung cancer is challenging, and a number of patients are already in the advanced stage of cancer when diagnosed, which markedly reduces the effectiveness of treatment. Meanwhile, the therapeutic effects of some traditional chemotherapy drugs, such as cisplatin, paclitaxel and carboplatin, remain very limited and exhibit high toxicity, leading to serious side effects (3). Accordingly, exploring the pathogenesis of NSCLC and discovering new effective treatment methods remain the main obstacles that need to be addressed.

Natural products derived from plants have been widely used since ancient times to prevent and treat various diseases. Low-toxicity, low-cost natural products with anticancer properties have always been of great concern (4,5). Quinones are an interesting class of compounds developed for the treatment of cancer, such as purpurin, lapachine and emodin (6-8), which are expected to be used in clinical adjuvant anticancer therapy to improve anticancer efficacy and reduce the toxic side effects of chemotherapy alone. Thymoquinone (TQ) (Fig. 1) is the primary substance that exerts biological effects in the volatile oil of the black seed (*Nigella sativa*) and has been widely used as an antibacterial, antiviral and hypoglycemic medicine for over two centuries (9,10). In addition, TQ has shown promising antitumor properties on several types of cancer cells. Zhao *et al* (11) discovered that TQ reduces the survival, migration and invasion of pancreatic cancer cells by regulating the PI3K/AKT/mTOR pathway. Taiyab *et al* (12) also reported the role of TQ in breast cancer, indicating that it inhibits cell proliferation and induces cell apoptosis. Recently, it has been proven that TQ markedly inhibited the proliferation of NSCLC (13). A significant feature is that TQ can induce cytotoxicity and apoptosis in cancer cells while being relatively non-toxic to normal cells (9,10). Based on the aforementioned research, it is not difficult to find that TQ may have broad-spectrum anticancer properties. However, due to its low bioavailability, TQ's poor aqueous solubility and photosensitivity severely restrict its biomedical application.

Therefore, various solubilizers and drug carriers are employed to promote the efficacy of hydrophobic drugs by increasing solubility and bioavailability (14,15). Among all solubility enhancement preparation methods, cyclodextrins (CDs) complexation to form drug-inclusion complexes has markedly improved the water solubility of lipophilic drugs, making it widely used in the pharmaceutical field (16). In

Correspondence to: Dr Ling Ye, Department of Radiation Oncology, Sun Yat-sen Memorial Hospital, Sun Yat-sen University, 33 Yingfeng Road, Guangzhou, Guangdong 510120, P.R. China
E-mail: zxc1378785@163.com

Key words: thymoquinone, hydroxypropyl-β-cyclodextrin, inclusion complex, non-small cell lung cancer, ferroptosis

addition, the CD inclusion process can also improve the pharmacological properties of these compounds, such as eliminating unpleasant odors and flavors (17). CDs are a class of cyclic oligosaccharides obtained from starch through enzymatic reactions, which are non-toxic and biodegradable under certain conditions. The microstructure of CDs presents a unique truncated cone shape consisting of a hydrophilic exterior surface and a hydrophobic interior cavity. When hydrophobic organic molecules enter the internal cavity of CDs, they form inclusion complexes. CDs are divided into three natural forms based on the number of pyranose glucose units: α-CD, β-CD and γ-CD (18). Among different CD family members, β-CD is widely used due to its easy availability and low cost. Hydroxypropyl-β-cyclodextrin (HP-β-CD), as a derivative of β-CD (Fig. 1), has been included in the GRAS list since 1998 as a fragrance carrier and protectant due to its higher solubility and more excellent biocompatibility (19). Subsequently, with the development of supramolecular functional materials, HP-β-CD has become a highly valuable and attractive nano-delivery carrier, widely used in anticancer agents. Previous research demonstrated that the encapsulation of paclitaxel by HP-β-CD can increase its dissolution rate, cytotoxicity and intracellular accumulation (20). Saha *et al* (21) reported that *trans*-resveratrol (RES) embedded in HP-β-CD exhibits more potent antitumor activity than free RES and its effect on preventing tumor growth *in vivo* is more significant. Early literature reported on the formation of inclusion complexes between TQ and different types of CDs (22-24), such as TQ/SBE-β-CD exhibiting enhanced water solubility and growth inhibitory effects on leukemia cells (24). However, to the best of the authors' knowledge, there is currently no literature on the growth inhibitory effect of this complex on tumors *in vivo*, let alone the specific mechanism by which TQ/CD complexes exert anticancer effects.

The present study comprehensively characterized the inclusion complex between TQ and HP-β-CD. The authors also analyzed the effects of pure TQ and the TQ/HP-β-CD inclusion complex on the growth and ferroptosis of NSCLC cells both *in vitro* and *in vivo*, as well as the possible signaling pathways involved (NF-κB pathway), which is a novel domain.

Materials and methods

Reagents. HP-β-CD (MW 1396), TQ (MW 164), ferroptosis inhibitor (Ferrostatin-1) and NF-κB activator (PMA) were purchased from Shanghai Aladdin Biochemical Technology Co., Ltd. Cell Counting Kit-8 (CCK-8) reagent (cat. no. AB0101), BeyoClick™ EdU-594 Kit (cat. no. C0071S), Hochest 33258 staining Kit (cat. no. C1011), DCFH-DA (cat. no. S0036S), dimethyl sulfoxide (DMSO) (cat. no. ST038), MDA Assay Kit (cat. no. S0131S), hematoxylin-eosin (H&E) staining Kit (cat. no. C02-04004), normal goat serum blocking solution (cat. no. P0260), HRP-labeled goat anti-rabbit secondary antibody (cat. no. A0181) and reduced glutathione (GSH) Assay Kit (cat. no. S0053) were obtained from Beyotime Institute of Biotechnology. C11-BODIPY 581/591 kit (cat. no. D3861) was obtained from Invitrogen; Thermo Fisher Scientific, Inc.. Anti-p-NF-κB (cat. no. ab207297) and anti-Ki-67 (cat. no. ab15580) were purchased from Abcam.

Preparation and characterization of TQ/HP-β-CD inclusion complex. TQ/HP-β-CD was prepared by the freeze-drying method following the protocol previously reported (22,23). TQ/HP-β-CD inclusion complex was characterized by Fourier transform infrared (FT-IR) spectrophotometry (Avatar 370, Thermo-Nicolet; Thermo Fisher Scientific, Inc.), Powder X-ray diffraction (XRD) (Shimadzu Corporation), differential scanning calorimetry (DSC) (3500 Sirius, NETZSCH Group), and scanning electron microscopy (SEM) (Nova Nano SEM 230; Thermo Fisher Scientific, Inc.) as previously reported (22-24).

Determination of phase solubility. The phase solubility study was conducted according to the methods described in previous literature (22). Briefly, excess TQ or TQ/HP-β-CD inclusion complex is added to distilled water with a pH of 7.0 and stirred continuously at 500 x g for 24 h at 37˚C. After filtering the suspension, the phase solubility is detected using an ultraviolet (UV)-visible spectrometer. The apparent stability constant (K) and complexation efficiency (CE) are calculated from the solubility diagram using the following equations: $K=Slope/S_0$. (1-Slope) and CE=Slope/(1-Slope). S_0 is the solubility of TQ in the absence of HP-β-CD, and Slope is the corresponding slope of the phase solubility diagram.

Determination of drug release rate in vitro. A total of 0.1 g of TQ and 0.94 g of TQ/HP-β-CD inclusion complex (containing 0.1 g of TQ) were added each to 50 ml of PBS (pH=7.4) and then stirred continuously at a speed of 100 x g for 24 h at 37˚C. At the predetermined time, 1 ml of the supernatant solution was removed and replaced with an equal volume of fresh medium. The drug release rate was determined by a UV-visible spectrometer and calculated using the following equation: Drug release rate (%)=D_1/D_2 x100%. D_1 is the amount of released drug within a certain period and D_2 is the total amount of drug.

Hemolytic compatibility assay. Heparin sodium was added to the collected fresh blood samples to prevent coagulation. The venous blood was divided into three layers after centrifuging at 2,000 x g for 5 min. The red blood cells were separated from plasma and the remaining red blood cells were washed three times with normal saline to remove residual white blood cells. After that, the red blood cells were diluted with normal saline to prepare a 4% red blood cell solution.

A total of 300 μl of TQ/HP-β-CD solution with different concentrations (50, 100, 200, 400, 800, 1,500, 3,000 μmol/l), 1.2 ml of erythrocyte solution, and 1.2 ml of saline were added to 5-ml centrifuge tubes. A total of 1.5 ml of 4% red blood cell solution and 1.5 ml of deionized water were added to the test tube of the positive control group. In total, 1.5 ml of 4% red blood cell solution and 1.5 ml of normal saline were added to the test tube of the negative control group. The test tube was incubated in a 37˚C constant-temperature incubator for 1 and 24 h, respectively. The tubes were centrifuged at a speed of 2,000 x g for 5 min to precipitate red blood cells. The absorbance value of the supernatant at 450 nm was detected with a microplate reader.

The hemolysis rate of the positive control group was set as 100%, and the hemolysis rate of the TQ/HP-β-CD group was calculated according to the following equation: Hemolysis rate (%)=(A_1/A_0) x100%. A_1 is the absorbance value of the

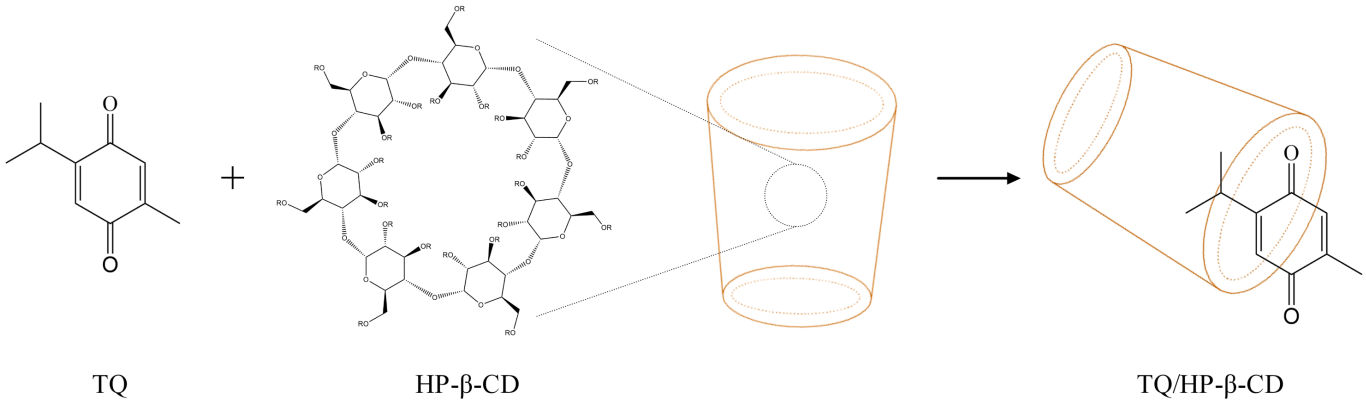

Figure 1. Schematic illustration of TQ/HP-β-CD inclusion complex. TQ, thymoquinone; HP-β-CD, hydroxypropyl-β-cyclodextrin

TQ/HP-β-CD group, and A_0 is the absorbance value of the positive control group.

Cell culture. Two immortalized NSCLC cell lines (A549 and HCC827) were obtained from the American Type Culture Collection and were incubated as previously described (11).

Cell uptake assessment. A549 cells were plated at a density of $5x10^4$ cells per well onto transparent microporous membrane inserts (Thincerts™; 1 μm pore size, 1.13 cm^2 surface area) within 12-well culture plates. Growth medium was introduced into the basolateral (1.0 ml) and apical (0.5 ml) compartments and refreshed at two-day intervals throughout a 21-day differentiation phase. Cultures were incubated at 37˚C with 90% humidity. Monolayers achieved experimental readiness when transepithelial electrical resistance stabilized within the 200-300 Ω·cm^2 range.

Both TQ solution and the TQ/HP-β-CD inclusion complex were diluted in Hanks' solution to yield equivalent final TQ concentrations of 25 μmol/l. These test formulations were apically administered to the differentiated monolayers. Permeability assessments commenced by adding 0.5 ml of test solution to the apical chamber and 1.0 ml of Hanks' solution to the basolateral chamber. Aliquots were periodically collected from the basolateral compartment for quantitative analysis via high performance liquid chromatography.

The apparent permeability coefficient (Papp, cm/s) was derived using the equation: Papp=dQ/(dt x A x C_0). dQ/dt is the steady-state permeation rate (mass/time), C_0 is the initial apical drug concentration, and A is the monolayer surface area (cm^2).

Cell viability assay. The increasing concentrations of TQ, HP-β-CD, and TQ/HP-β-CD in the treatment group were 12.5, 25, 50, 100, 200, 300, and 400 μmol/l. TQ was dissolved in DMSO to prepare a 50 mmol/l mother solution.

Different concentrations of TQ samples were obtained by diluting the mother liquor with a DMEM medium and labeling it as the TQ/DMSO group. TQ was dissolved in a DMEM medium to obtain TQ samples of different concentrations labeled as TQ/H_2O group. HP-β-CD was dissolved in a DMEM medium to obtain different concentrations of HP-β-CD samples, which were labeled as the HP-β-CD group. TQ/HP-β-CD inclusion complex was dissolved in DMEM medium to obtain TQ/HP-β-CD samples of different concentrations, labeled as TQ/HP-β-CD group.

A total of $1x10^4$ A549 or HCC827 cells were cultivated in 96-well plates with different concentrations of TQ, HP-β-CD, and TQ/HP-β-CD as aforementioned for 24 h. A total of 10 μl of CCK-8 reagent was added to each well of a 96-well plate, followed by incubation at 37˚C for 1 h, and the absorbance value was detected at 570 nm with a microplate reader. The value of IC_{50} was analyzed using GraphPad software 8.0 software (Dotmatics). The growth inhibitory rate was calculated according to the following equation: Growth inhibitory rate (%)=(1-A_1/A_0) x100%. A_1 is the absorbance value of the treatment group, and A_0 is the absorbance value of the negative control group.

5-Ethynyl-2'-deoxyuridine (EdU) assay. A549 or HCC827 cells at logarithmic growth phase were inoculated into a 96-well plate and treated with different drugs for 24 h. EdU working solution was added and cells remained for 2 h in a 37˚C incubator. Pre-cooled 4% paraformaldehyde was added, and cells were incubated at room temperature for 30 min. A total of 0.5% Triton X-100 was used to permeate the membrane for 20 min and react with Hoechst 33342 reaction solution in the dark for 30 min. Finally, the image was analyzed using ImageJ software (version 1.51j8; National Institutes of Health).

Collagen sprout outgrowth assay. The proliferation and migration activities were measured in A549 or HCC827 cells by the collagen sprout outgrowth assay as previously described (25).

Reactive oxygen species (ROS) detection. A549 or HCC827 cells at logarithmic growth phase were inoculated into a 6-well plate, treated with different drugs for 24 h at 37˚C, and then washed three times with PBS. Then, ROS was measured using fluorescence microscopy and flow cytometry, respectively. DCFH-DA was used to detect the ROS levels according to the manufacturer's protocol. In brief, A549 or HCC827 cells at logarithmic growth phase were seeded in 6-well plates and cultured with different drugs for 24 h at 37˚C. After treatment, cells were harvested and washed three times with PBS and labeled with 20 μmol/l DCFH-DA under 37˚C for 30 min in the dark. The cells were then washed with PBS, followed by fluorescence microscopy imaging (Zeiss LSM800; Zeiss GmbH). ROS levels were detected using BD FACS-Calibur

flow cytometer (BD Biosciences), and the fluorescence intensity of ROS was analyzed with FlowJo software (FlowJo LLC).

Detection of lipid peroxidation. The level of lipid peroxidation in $1.0x10^5$ A549 or HCC827 cells was measured using the C11-BODIPY 581/591 kit according to the manufacturer's protocol.

Measurement of malondialdehyde (MDA) and GSH/ oxidized glutathione (GSSG) ratio. After $2.0x10^5$ A549 or HCC827 cells were treated with different drugs for 24 h, the content of MDA and GSH/GSSG ratio were determined according to the manufacturer's protocol.

Electrophoretic mobility shift assay (EMSA). Nuclear extracts were extracted from A549 cells and incubated with IRDye-700-labeled NF-κb oligonucleotides for electrophoretic mobility shift assay, as previously described (26).

Mouse xenograft model. A total of 15 female BALB/c nude mice (6 weeks old, ~22 g) were purchased from Beijing Weitong Lihua Company. Animals were housed under specific pathogen-free conditions at a controlled temperature of 22±2˚C, 50±10% relative humidity, and a 12/12-h light-dark cycle with ad libitum access to autoclaved water and standard rodent chow. Environmental enrichment (for example, nesting material and shelters) was provided. All animal experiments followed the ARRIVE guidelines and were approved (approval no. 20240215001) by the Animal Care and Ethics Committee of Ma'anshan People's Hospital (Ma'anshan, China) conducted in strict accordance with the UK Animals (Scientific Procedures) Act 1986 and relevant institutional guidelines.

Each mouse was subcutaneously injected with $5x10^6$ A549 cells under brief isoflurane anesthesia (4% induction, 2% maintenance in oxygen). Tumor size was measured daily using digital calipers with volume calculated as (Length x Width^2)/2. Animal health and behavior (posture, mobility, grooming, spontaneous activity, and signs of pain/distress) were assessed twice daily throughout the study. Pre-defined humane endpoints requiring immediate euthanasia included: Tumor volume >1,500 mm^3, tumor ulceration or necrosis >15% surface area, body weight loss >20% from baseline, inability to access food/water, or severe lethargy/distress.

When tumors reached ~100 mm^3, mice were randomly assigned to treatment groups (n=5/group): untreated control, TQ group, or TQ/HP-β-CD group. The experimental duration post-grouping was 28 days. The TQ group received intraperitoneal injections of 100 µl solution containing 3 mg TQ every other day. The TQ/HP-β-CD group received intraperitoneal injections of 100 µl solution containing 28.2 mg TQ/HP-β-CD (equivalent to 3 mg TQ) every other day. The control group received no treatment. All mice survived to the scheduled endpoint. On day 28, mice were euthanized by cervical dislocation under deep isoflurane anesthesia (5% induction in oxygen). Death was confirmed by absence of detectable heartbeat (cardiac palpation), absence of respiratory movements for >5 min, and fixed dilated pupils. Liver, kidney and tumor tissues were immediately collected post-mortem for analysis. Welfare considerations included: i) Anesthesia for tumor implantation and euthanasia (isoflurane: 4% induction/2% maintenance for implantation; 5% for euthanasia) ii) strict humane endpoints iii) twice-daily health monitoring iv) environmental enrichment and v) minimized injection volumes. No analgesics were administered during treatment as injections caused only transient discomfort without observable distress. No animals required early euthanasia or were found dead during the study.

Histopathology and immunohistochemistry (IHC). The liver, kidney, and tumor tissues were placed in 4% paraformaldehyde for 48 h. Then, the tissues were embedded in paraffin and cut into thin slices (4 µm). Routine H&E and Perl staining were then performed on the slices. IHC for Ki-67 and NF-κb as also performed on paraffin-embedded tissue sections. Paraffin-embedded tissue sections were baked at 65˚C, dewaxed, hydrated, and subjected to antigen retrieval using citrate sodium buffer. Endogenous peroxidase activity was blocked with 3% H_2O_2. Sections were blocked with normal goat serum blocking solution at room temperature for 30 min. Primary antibodies were then applied: Ki-67 (1:200) or NF-κB p65 (1:100), and incubated at 4˚C overnight. After washing with PBS, HRP-labeled goat anti-rabbit secondary antibody (1:200) was added and incubated at room temperature for 1 h. DAB was used for color development, followed by counterstaining with hematoxylin. Finally, the sections were dehydrated, cleared, and mounted. Slices were observed and images were captured using an Olympus BX41 optical microscope (Olympus Corporation).

Statistical analysis. Three independent experiments were conducted, with data presented as the mean ± SD of absolute values or control percentages. Statistical analysis was conducted using GraphPad Prism 8.0 software (Dotmatics). The differences between two or more groups were confirmed through one-way ANOVA followed by Tukey's post hoc test. P-<0.05 (on both sides) was considered to indicate a statistically significant difference.

Results

Physicochemical characterization of TQ/HP-β-CD. Based on previous studies (22,23), the freeze-drying method was employed in the present study to prepare TQ/HP-β-CD inclusion complexes in a 1:1 molar ratio and characterize and biologically validate them.

FT-IR. In previous studies, FTIR was used to investigate the interaction between guest molecules and CDs in inclusion complexes (22-24). The FTIR spectra of TQ, HP-β-CD and TQ/HP-β-CD are demonstrated in Fig. 2A. HP-β-CD spectrum has unique absorption signals at ~3,318 cm^{-1} and 1,020 cm^{-1}, representing OH group and C-O-C glucose unit bending, respectively. Pure TQ exhibits an intense sharp band at 1,647 cm^{-1}, corresponding to the stretching of carbonyl groups. CH_2 produces stretching vibration displayed at 2,970 cm^{-1}. The spectral band of 1,450-1,020 cm^{-1} represents C=C bending vibration (aliphatic) and C-O-C stretching vibration. After the formation of the TQ/HP-β-CD inclusion complex, it can be observed that the carbonyl group of TQ located at 1,520 cm^{-1} disappears from the spectrum of the inclusion complex due to stretching. Meanwhile, the characteristic broad band of the OH groups in HP-β-CD shifted from 3,318 cm^{-1} to 3,401 cm^{-1}.

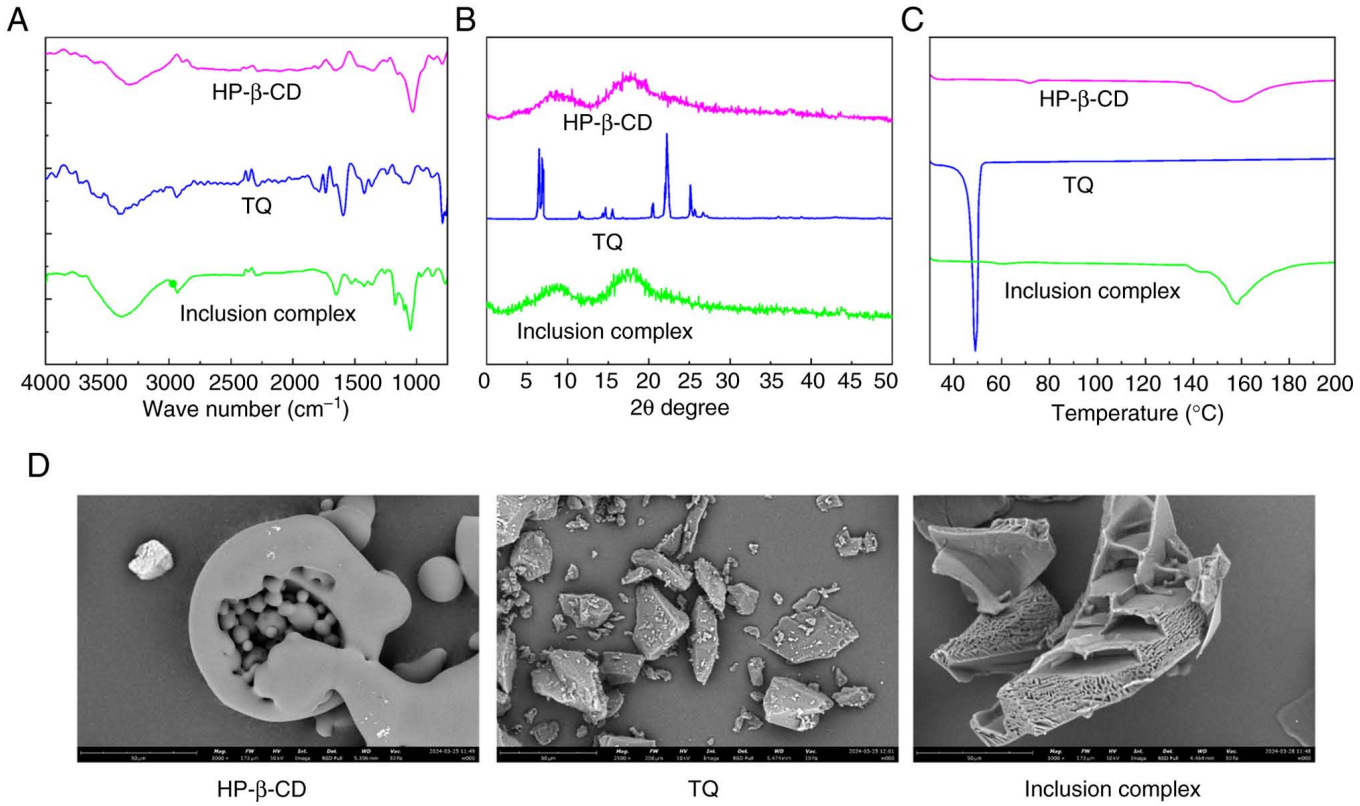

Figure 2. Characterization of TQ/HP-β-CD inclusion complex. (A) The Fourier transform infrared spectra, (B) X-ray diffraction diagram, (C) Differential scanning calorimetry and (D) scanning electron microscope images of TQ, HP-β-CD and TQ/HP-β-CD inclusion complex. TQ, thymoquinone; HP-β-CD, hydroxypropyl-β-cyclodextrin.

The signal changes related to the polar functional groups of TQ and HP-β-CD can indicate the partial embedding of TQ into the HP-β-CD cavity, thereby confirming the successful formation of the inclusion complex (Fig. 1).

XRD. As revealed in Fig. 2B, XRD was used further to investigate the inclusion complex of TQ and HP-β-CD. No diffraction peaks in the X-ray spectrum of HP-β-CD indicate that it is amorphous. The XRD pattern of TQ showed a series of strong and sharp diffraction peaks, indicating that the compound is essentially crystalline. However, the inclusion complex of TQ with HP-β-CD exhibited a well-differentiated diffusion X-ray pattern similar to HP-β-CD, indicating that TQ no longer exists in crystalline form and its inclusion complex with HP-β-CD exists in an amorphous state. The transformation into an amorphous form is important evidence for TQ to be embedded in the HP-β-CD cavity in a molecular state (20,21).

DSC. The DSC curves of TQ, HP-β-CD and TQ/HP-β-CD inclusion complex are shown in Fig. 2C. The DSC spectrum of HP-β-CD showed two peaks at 72 and 158˚C, corresponding to the glass transition (Tg) and melting point (Tm) temperatures, respectively. TQ has a sharp endothermic peak at 48.44˚C, which is the Tm of the crystal. The DSC spectrum of the TQ/HP-β-CD inclusion complex is highly similar to the HP-β-CD, but the difference is that the TQ/HP-β-CD inclusion complex has lower Tg and Tm. In addition, the endothermic peak of TQ disappeared in the DSC curve of the inclusion complex, which is attributed to the transition of crystalline TQ to an amorphous state. The aforementioned results indicated that the TQ/HP-β-CD inclusion complex exhibits reduced thermal stability and crystallization trend, consistent with the XRD results.

SEM. Under a scanning electron microscope (Fig. 2D), HP-β-CD exhibits an amorphous spherical structure with cavities. TQ presents an irregularly sized rectangular crystal structure, and inclusion complexes exhibited irregularly shaped aggregates or clumps. The change in the morphology of the inclusion complex is mainly attributed to the embedding of partial TQ molecules into the cavity of HP-β-CD, which confirms the formation of the inclusion complex morphologically, similar to previous literature (21).

Solubility detection. The phase solubility diagram of TQ encapsulated into HP-β-CD was depicted in Fig. 3A, indicating that the water solubility of TQ increases proportionally with the increase of HP-β-CD molar concentration. The correlation coefficient (R^2) of the linear regression equation is 0.98, showing that the system follows an A_L-type solubility plot. The apparent stability constant ($K_{1:1}$) of the inclusion complex is related to its stability. The $K_{1:1}$ value increases proportionally to the stability of the inclusion complex (24). The $K_{1:1}$ value of the TQ/HP-β-CD inclusion complex is 562.34 l/mol, demonstrating the preparation of a stable inclusion complex between HP-β-CD and TQ. The detection of solubility at room temperature (26˚C) demonstrated that the solubility of TQ and TQ/HP-β-CD inclusion complex in aqueous solution

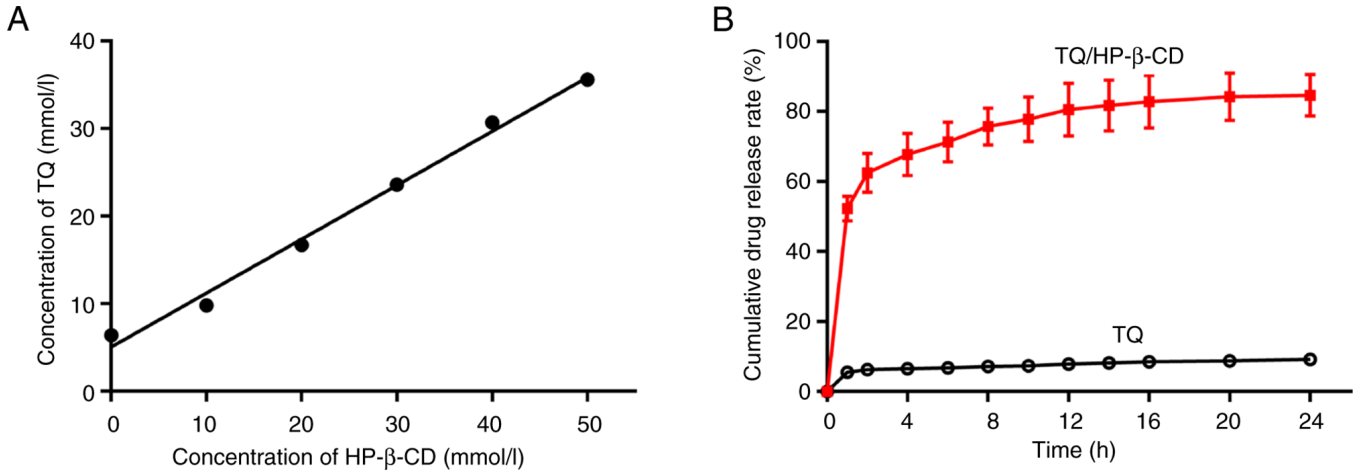

Figure 3. (A) Phase solubility diagram of TQ/HP-β-CD host-guest system. (B) *In vitro* release curve of free TQ and TQ/HP-β-CD inclusion complex in PBS (pH=7.4 at 37˚C). TQ, thymoquinone; HP-β-CD, hydroxypropyl-β-cyclodextrin

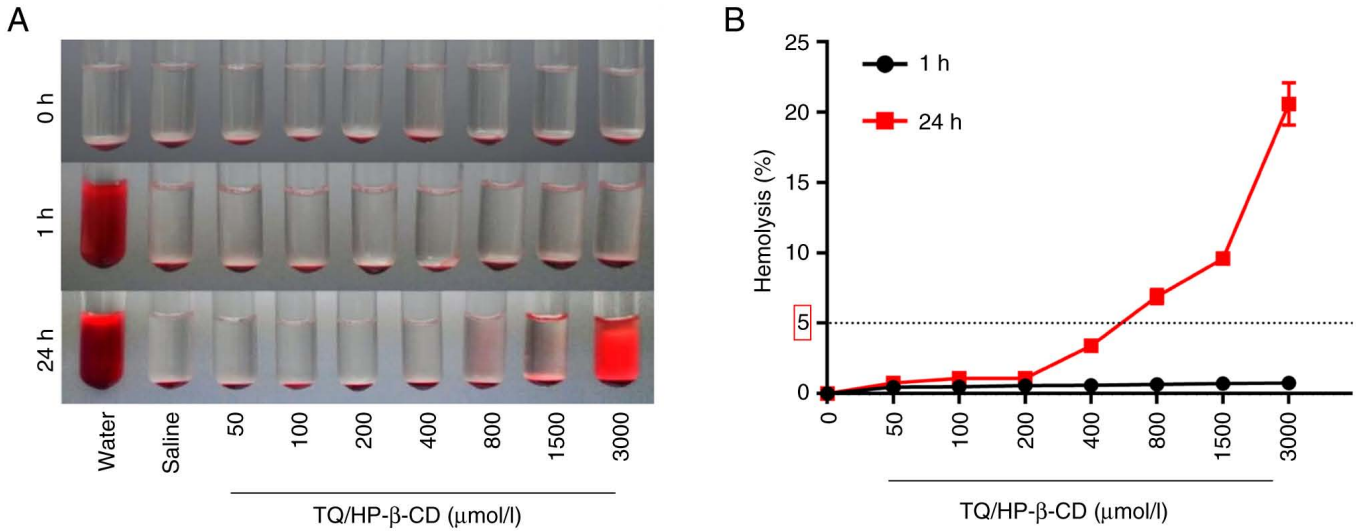

Figure 4. (A) Hemocompatibility of TQ/HP-β-CD inclusion complex. Effect of different concentrations of TQ/HP-β-CD inclusion complex on red blood cell hemolysis after 1 h and 24 h of treatment. (B) Spectrophotometry was used to quantitatively evaluate the degree of hemolysis in each group. TQ, thymoquinone; HP-β-CD, hydroxypropyl-β-cyclodextrin.

were 0.024 and 37.42 mmol/l, respectively. The solubility of TQ/HP-β-CD was 1,559-fold that of TQ. The CE displays the ratio of dissolved complex concentration to dissolved free CD concentration and was employed to evaluate the solubility of hydrophobic molecules in CDs (27). According to the phase solubility diagram, the CE value of the inclusion complex is 1.942, indicating HP-β-CD is suitable for preparing TQ.

In vitro release behavior of TQ. To investigate whether the surface modifier HP-β-CD can enhance the hydrophilicity of TQ as well as improve the release characteristics of TQ. Then, the *in vitro* release experiment of TQ was performed. The *in vitro* drug release curves of free TQ and TQ/HP-β-CD inclusion complex in PBS (pH=7.4) at 37˚C for ~24 h were displayed in Fig. 3B. Specifically, the cumulative amount of TQ released from the TQ/HP-β-CD inclusion complex increased rapidly in the first h of the experiment, gradually increasing and reaching a plateau. A total of >52.5% of TQ was released from the inclusion complex within the first h, while free TQ was only released at 5.5%. After 24 h, the drug release rate in inclusion complex and free TQ were 84.3 and 9.3%, respectively. The aforementioned data confirmed the ability of the new formula (TQ/HP-β-CD) to improve the hydrophilicity and release characteristics of TQ.

Blood hemolysis evaluation of TQ/HP-β-CD. According to the national evaluation standard (GB/T16886.4-2003), the hemolysis rate of medical biomaterials used in clinical applications should be <5% to meet the safety requirements of biomaterials (28). As demonstrated in Fig. 4A, the upper liquid of the test tube in the negative control group is clear and transparent, and erythrocytes precipitate at the bottom, indicating that hemolysis has not occurred. After 1 h of reaction, the upper liquid of the test tube in the positive control group was uniformly red, and there was no red blood cell precipitation at the bottom, indicating that all red blood cells had

undergone hemolysis. After treatment with different concentrations of TQ/HP-β-CD inclusion complex (50-3,000 μmol/l) for 1 h, the test tube solution remained relatively clear. When the processing time of the inclusion complex was extended to 24 h, the test tube liquid of the low concentration TQ/HP-β-CD inclusion complex (50-400 μmol/l) group remained clear, while the upper liquid of the test tube of the high concentration TQ/HP-β-CD inclusion complex (800-3,000 μmol/l) group appeared red, indicating that the low concentration TQ/HP-β-CD inclusion complex (50-400 μmol/l) used in the present study had favorable blood compatibility.

In addition, the hemolysis degree of each group was quantitatively measured using spectrophotometry (Fig. 4B). The results showed that after 1 h of treatment, the hemolysis rate of the TQ/HP-β-CD groups with different concentrations was <1%. When the action time of the TQ/HP-β-CD is extended to 24 h, the red blood cell hemolysis rate of the low concentration TQ/HP-β-CD groups (50-400 μmol/l) is <5%. When the concentration of the TQ/HP-β-CD exceeds 400 μmol/l, the red blood cell hemolysis rate exceeds the threshold of 5%, indicating that the low-concentration inclusion complex inflicts damage to red blood cells and meets the safety requirements of national standards. The concentration of TQ/HP-β-CD inclusion complex used in subsequent experiments is within the safe range.

In vitro permeability study. To investigate the potential of HP-β-CD to enhance the permeability and subsequent cellular uptake of TQ in A549 cells, permeability studies were conducted comparing free TQ to the TQ/HP-β-CD inclusion complex. The Papp values determined were $1.04x10^{-7}$ cm/s for free TQ and $5.2x10^{-7}$ cm/s for the TQ/HP-β-CD complex. This 5-fold increase in Papp demonstrates that complexation with HP-β-CD significantly enhances the transepithelial transport and cellular uptake of TQ in the A549 monolayer model. These findings indicate that HP-β-CD serves as an effective carrier system, facilitating the delivery of a greater amount of TQ into tumor cells.

TQ/HP-β-CD suppressed cell proliferation and migration in NSCLC cells. Previous studies have confirmed that TQ significantly inhibits the proliferation, migration and invasion of various human cancer cells, including lung cancer (11-13). Meanwhile, compared with free TQ, the nano-emulsion loaded with TQ has higher cellular uptake and more potent anticancer activity (27). The present study compared the inhibitory effects of TQ/H_2O, TQ/DMSO, HP-β-CD and TQ/HP-β-CD inclusion complex on the proliferation of NSCLC cell lines, specifically A549 and HCC827 cells. As shown in Fig. 5A, TQ/DMSO exerted a strong inhibitory effect on the proliferation of A549 and HCC827 cells, with IC_{50} values of 26.1 and 28.2 μmol/l, respectively, which are similar to previous findings (13). TQ/H_2O revealed a weaker inhibitory effect on the proliferation of A549 and HCC827 cells, with IC_{50} values of 290.6 and 252.2 μmol/l, respectively. The inhibition rate of HP-β-CD on the proliferation of NSCLC cells was <3%, indicating that HP-β-CD was almost non-toxic. Combining TQ with HP-β-CD to form an inclusion complex had a stronger inhibitory effect on the proliferation of NSCLC cells than TQ/H_2O, with IC_{50} values reduced to 48.2 and 61.7 μmol/l, respectively. This enhanced inhibitory activity aligns with the significantly improved permeability and cellular uptake of TQ/HP-β-CD observed in the A549 monolayer model, where its apparent permeability coefficient (Papp) was 5-fold higher than that of free TQ.

The EdU assay results showed that TQ/H_2O could effectively inhibit the proliferation of A549 and HCC827 cells (Fig. 5B), and the inhibitory effect of TQ/HP-β-CD at the same concentration on NSCLC cell proliferation was further enhanced. In addition, the collagen sprout outgrowth assay is an effective method for evaluating cell proliferation and migration, with longer buds indicating more vigorous cell proliferation and migration abilities (29). As shown in Fig. 5C, TQ/H_2O significantly inhibited the sprout outgrowth of A549 and HCC827 cells after 24 h of treatment. Compared with TQ/H_2O, the sprout length of A549 and HCC827 cells treated with TQ/HP-β-CD was further shortened.

The aforementioned results indicate that HP-β-CD can enhance the inhibitory effect of TQ on the proliferation and migration of NSCLC cells. Considering the excellent biocompatibility of TQ/HP-β-CD in the experimental concentration range, TQ/HP-β-CD can potentially become an anti-tumor agent for treating NSCLC.

TQ/HP-β-CD induces ferroptosis in NSCLC cells. To confirm whether TQ/HP-β-CD can induce ferroptosis in NSCLC cells, DHCA staining was first used to detect the generation of ROS. The results showed that TQ/HP-β-CD treatment increased ROS generation in A549 and HCC827 cells (Fig. 6A). Flow cytometry further showed that TQ/HP-β-CD increases the expression of ROS in NSCLC cells (Fig. 6B).

In addition, the present study further detected the hallmark of ferroptosis - lipid peroxidation level-in NSCLC cells. The dye C11-BODIPY 581/591 was used, which is sensitive to lipid peroxidation, for laser confocal scanning microscopy observation. The intensity of green fluorescence (oxidized C11-BODIPY) under the microscope was used to evaluate the level of lipid peroxidation. The results revealed that TQ/HP-β-CD treatment increased lipid peroxidation levels in A549 and HCC827 cells (Fig. 6C). Meanwhile, the level of lipid peroxidation product MDA in A549 and HCC827 cells was increased after TQ/HP-β-CD treatment. The present study found that TQ/HP-β-CD can significantly downregulate the level of GSH and the ratio of GSH/GSSG in NSCLC cells (Fig. 6D). These data indicated that TQ/HP-β-CD can induce ferroptosis in A549 and HCC827 cells.

Ferroptosis-dependent effect of TQ/HP-β-CD against NSCLC cells. To further verify that ferroptosis is the main form of TQ/HP-β-CD induced NSCLC cell death, rescue experiments were conducted by Ferrostatin-1, a widely used ferroptosis inhibitor. It was found that Ferrostatin-1 can effectively alleviate the inhibitory effect of TQ/HP-β-CD on the proliferation of A549 and HCC827 cells (Fig. 7A). Meanwhile, pretreatment with Ferrostatin-1 can also reverse the accumulation of ROS mediated by TQ/HP-β-CD in the cytoplasm (Fig. 7B) and the increase in lipid peroxidation level (Fig. 7C). In addition, ELISA experiments identified that Ferrostatin-1 can effectively restore the elevated MDA level and decreased GSH level induced by TQ/HP-β-CD in A549 and HCC827 cells (Fig. 7D).

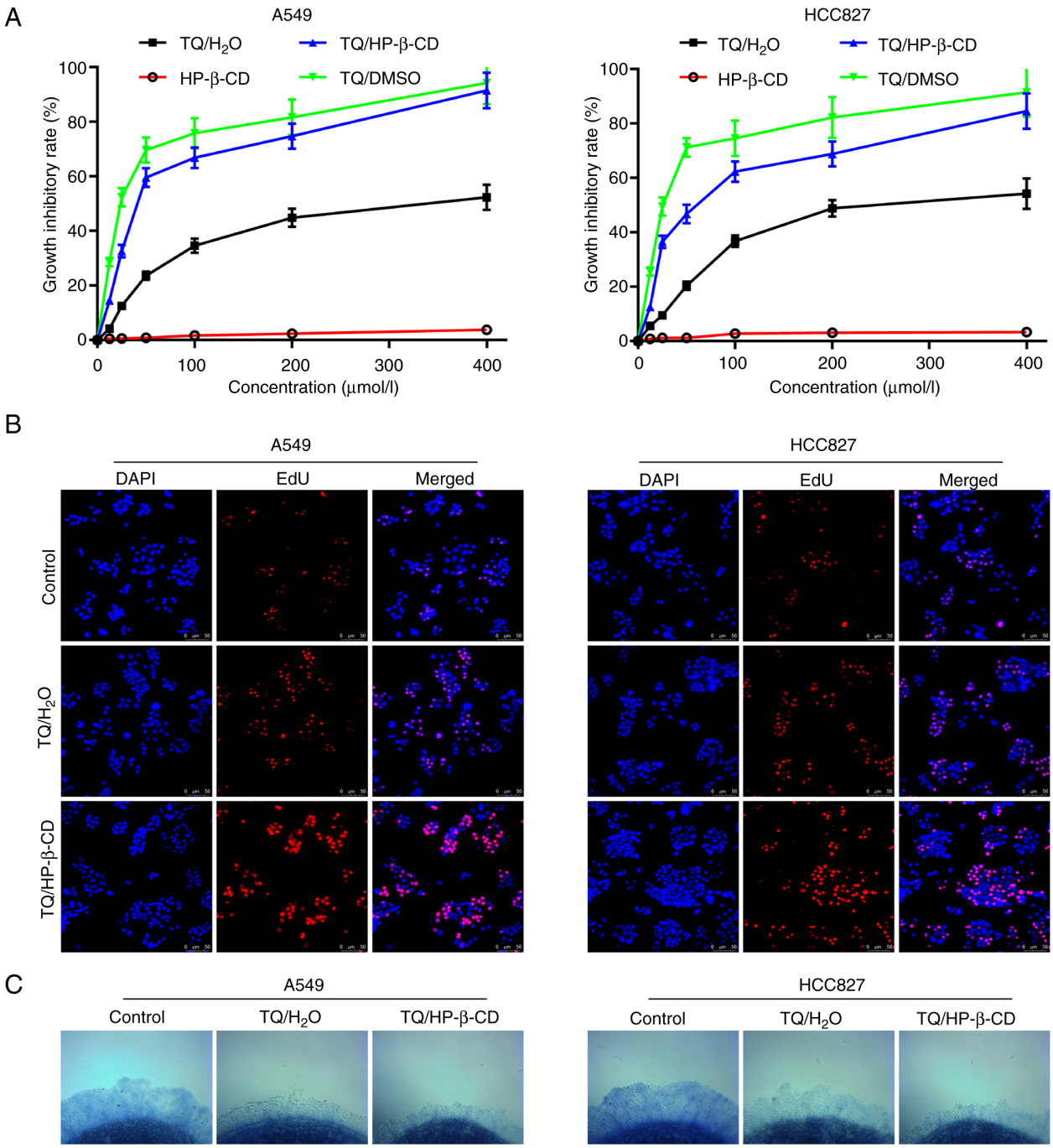

Figure 5. (A) The growth inhibitory effect of TQ/H_2O, TQ/DMSO, HP-β-CD and TQ/HP-β-CD inclusion complex on A549 and HCC827 cells was determined by Cell Counting Kit-8 assay. (B) Cell proliferation capacity was detected by EdU staining after treatment with TQ/H_2O and TQ/HP-β-CD for 24 h in non-small-cell lung cancer cells. (C) The effects of TQ/H_2O and TQ/HP-β-CD on the sprout outgrowth of A549 and HCC827 cells. TQ, thymoquinone; HP-β-CD, hydroxypropyl-β-cyclodextrin.

NF-κb is a key regulatory factor in TQ/HP-β-CD mediated ferroptosis. To elucidate the underlying mechanism by which TQ/HP-β-CD induces ferroptosis, NF-κB DNA binding activity was measured using EMSA (Fig. 8A). The results showed that treatment with TQ/HP-β-CD alone for 24 h effectively suppressed NF-κB DNA binding activity. To further investigate the dependence of TQ/HP-β-CD-induced ferroptosis on NF-κB, A549 cells were pretreated with the NF-κB activator PMA followed by TQ/HP-β-CD treatment. Notably, PMA pretreatment rescued the inhibitory effect of TQ/HP-β-CD on NF-κB activity.

Subsequently, the CCK-8 assay results indicated that PMA can partially reverse the inhibitory effect of TQ on A549 cell proliferation (Fig. 8C). Meanwhile, after TQ/HP-β-CD treatment, lipid peroxidation level and ROS generation increased in A549 cells. At the same time, PMA successfully weakened the effect of TQ/HP-β-CD on lipid peroxidation and ROS generation (Fig. 8B and D). In addition, PMA also alleviated the regulatory effect of TQ/HP-β-CD on the expression of MDA and GSH in A549 cells (Fig. 8E). The aforementioned results indicated that TQ/HP-β-CD may first inhibit the basal level of NF-κB DNA binding activity previously present in NSCLC cells, leading to

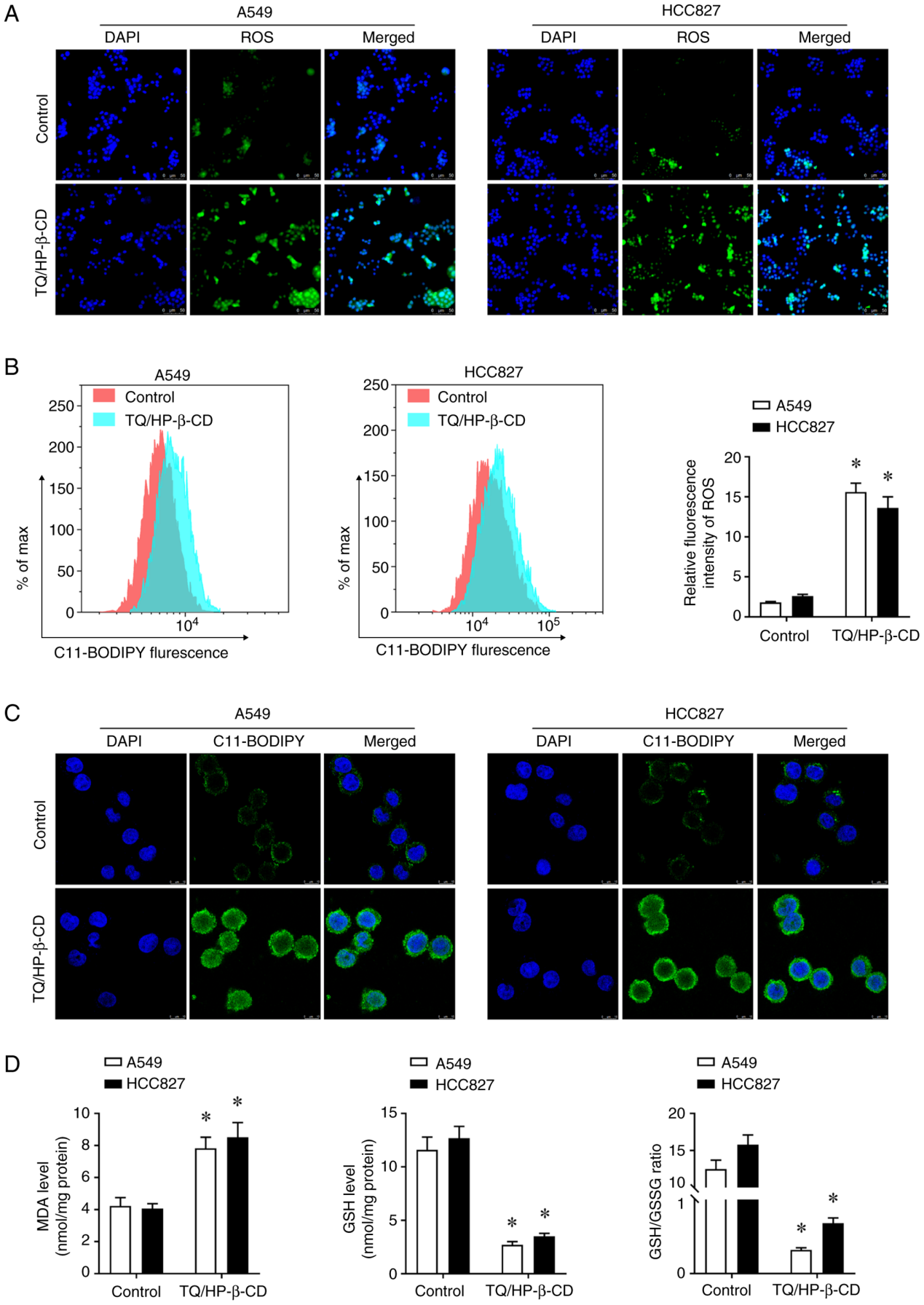

Figure 6. TQ/HP-β-CD induces ferroptosis in NSCLC cells. The effect of TQ on ROS generation in NSCLC cells was detected by (A) DHCA staining and (B) flow cytometry. (C) Detection of lipid peroxidation level in NSCLC cells by C11-BODIPY 581/591 staining. (D) The levels of MDA, GSH and the ratio of GSH/GSSG in NSCLC cells were detected by ELISA. *P<0.05 vs. control group. TQ, thymoquinone; HP-β-CD, hydroxypropyl-β-cyclodextrin; NSCLC, non-small-cell lung cancer; MDA, malondialdehyde; GSH, reduced glutathione; GSSG, oxidized glutathione.

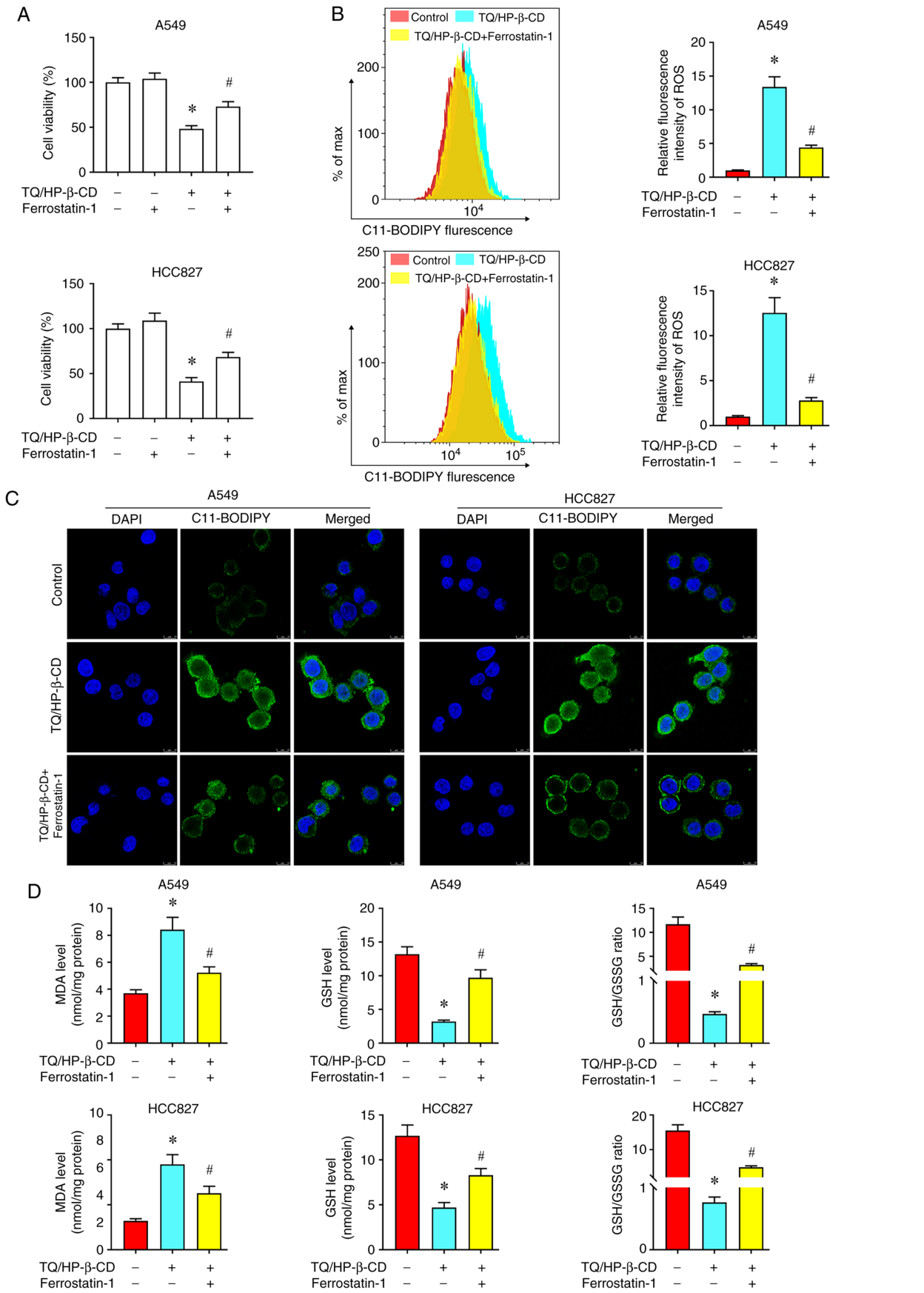

Figure 7. Ferroptosis-dependent effect of TQ/HP-β-CD against NSCLC cells. Cell viability detection in A549 and HCC827 cells treated with or without Ferrostatin-1 in the presence of TQ/HP-β-CD (A). Analysis of ROS level in A549 and HCC827 cells treated with or without Ferrostatin-1 in the presence of TQ/HP-β-CD (B). Detection of lipid peroxidation level in NSCLC cells treated with or without Ferrostatin-1 in the presence of TQ/HP-β-CD (C). The levels of MDA, GSH and the ratio of GSH/GSSG in NSCLC cells were detected by ELISA. (D) *P<0.05 vs. control group; #P<0.05 vs. TQ/HP-β-CD group. TQ, thymoquinone; HP-β-CD, hydroxypropyl-β-cyclodextrin; NSCLC, non-small-cell lung cancer; MDA, malondialdehyde; GSH, reduced glutathione; GSSG, oxidized glutathione.

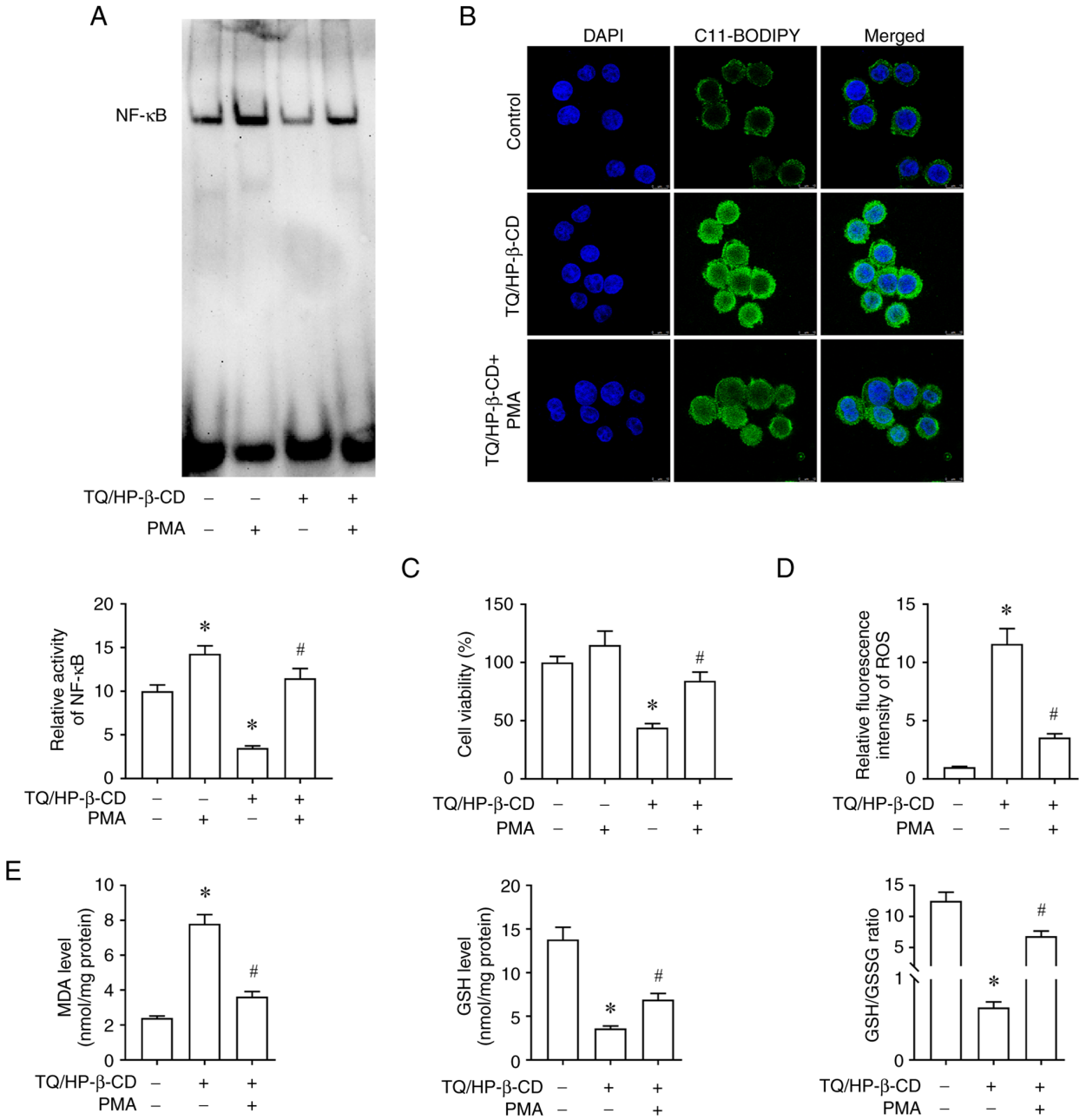

Figure 8. TQ/HP-β-CD induces ferroptosis in non-small-cell lung cancer cells by inhibiting NF-κB activity. (A) Electrophoretic mobility shift assay showing NF-κB DNA binding activity in A549 cells. (B) Detection of lipid peroxidation level in A549 cells. (C) Cell viability of A549 and HCC827 cells was determined by Cell Counting Kit-8 assay. (D) Analysis of ROS level in A549 cells. (E) The levels of MDA, GSH and the ratio of GSH/GSSG in A549 cells were detected by ELISA. *P<0.05 vs. control group; #P<0.05 vs. TQ/HP-β-CD group. TQ, thymoquinone; HP-β-CD, hydroxypropyl-β-cyclodextrin; ROS, reactive oxygen species; MDA, malondialdehyde; GSH, reduced glutathione; GSSG, oxidized glutathione.

the inactivation of downstream genes and ultimately inducing ferroptosis in NSCLC cells. However, the exact mechanism by which TQ/HP-β-CD regulates the NF-κB pathway in NSCLC cells remains unclear, and further research is needed to determine whether other molecular mechanisms are involved.

In vivo antitumor efficacy and safety of TQ/HP-β-CD. In the A549 xenograft mouse model, both TQ and TQ/HP-β-CD significantly inhibited tumor growth compared with the control group. The tumor growth inhibition rates were 32.1% for TQ and 67.9% for TQ/HP-β-CD (Fig. 9A and B). H&E staining of tumor tissues revealed more extensive necrotic features (nuclear fragmentation, contraction and dissolution) in the TQ/HP-β-CD group compared with TQ and control groups (Fig. 9E). IIHC showed a significant reduction in Ki-67 positive cells (indicating proliferation) in TQ/HP-β-CD treated tumors compared with both control and TQ groups (Fig. 9F).

Furthermore, mice treated with TQ or TQ/HP-β-CD showed no significant adverse symptoms (vomiting, convulsions or bloating) and maintained stable body weights (Fig. 9C). H&E staining of liver and kidney tissues from all groups revealed normal architecture without significant pathological changes (Fig. 9E).

Induction of ferroptosis in vivo. Analysis of subcutaneous tumors showed that both TQ and TQ/HP-β-CD treatment

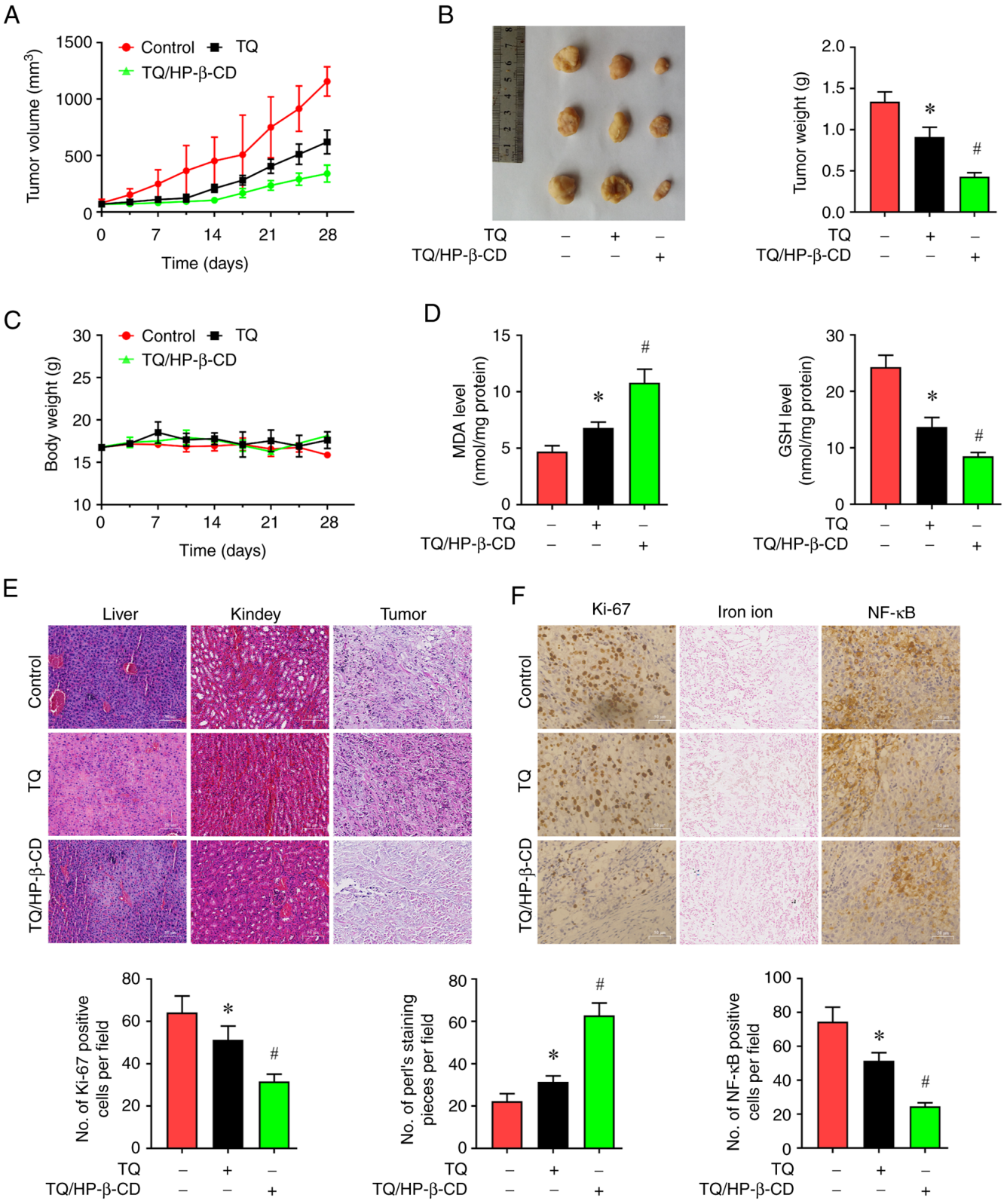

Figure 9. TQ/HP-β-CD triggers ferroptosis in the xenograft model of non-small-cell lung cancer. After treatment with TQ and TQ/HP-β-CD in subcutaneous transplanted tumors, (A) the growth curve, (B) tumor weight and (C) nude mouse weight were measured. (D) ELISA method was used to detect the levels of MDA and GSH in subcutaneous transplanted tumors. (E and F) Representative images of H&E staining in liver, kidney, and tumor tissues were used to evaluate the expression levels of Ki67 and NF-κB through immunohistochemical staining. Prussian blue staining was used to detect free iron deposition in tissues. *P<0.05 vs. control group; #P<0.05 vs. TQ group. TQ, thymoquinone; HP-β-CD, hydroxypropyl-β-cyclodextrin.

significantly decreased GSH levels and increased MDA levels compared with the control group, with TQ/HP-β-CD showing a stronger effect (Fig. 9D). Prussian blue staining revealed significantly increased free iron deposition in tumor tissues from both TQ and TQ/HP-β-CD treated mice compared with controls, again more pronounced in the complex group (Fig. 9F).

IHC analysis showed significantly reduced positive expression of NF-κB in tumor tissues from TQ and TQ/HP-β-CD groups compared with control, with TQ/HP-β-CD exhibiting a stronger suppressive effect (Fig. 9F).

In summary, *in vivo* research results indicated that TQ/HP-β-CD has favorable biocompatibility and a stronger inhibitory effect on NSCLC growth than TQ, and NF-κB-mediated ferroptosis induction may be its primary mechanism of action, which is consistent with *in vitro* experimental results.

Discussion

The present study established a novel TQ/HP-β-CD inclusion complex (TQ/HP-β-CD) via freeze-drying. Structural characterization by FT-IR, XRD, DSC and SEM confirmed successful TQ encapsulation within the HP-β-CD cavity. The complex significantly enhanced TQ's aqueous solubility (1,559-fold) and bioavailability, translating to potent anti-NSCLC activity both *in vitro* and *in vivo*. This directly addresses TQ's primary clinical limitation: Free TQ's poor water solubility fundamentally restricts its contact with cancer cells, explaining the weak growth inhibition observed in aqueous formulations. While DMSO improves TQ solubility and cytotoxicity by facilitating molecular contact, its solvent properties preclude clinical translation and fail to reflect physiological drug behavior.

By contrast, the TQ/HP-β-CD complex achieves superior anticancer efficacy through dual mechanisms: i) exceptional water solubility delivers more bioactive TQ molecules to tumor cells, and ii) cyclodextrin-mediated transport enhances membrane permeability-synergistically overcoming pharmaceutical barriers constraining natural products (22). As a nano-scale delivery system, HP-β-CD leverages critical advantages: Reduced particle size facilitates cellular internalization, enables higher therapeutic dosing without solvent toxicity, and minimizes drug loss from first-pass metabolism and P-glycoprotein efflux (30). These properties potentiate TQ's bioactivity and align with evidence that nanoparticle formulations can trigger ferroptosis, an iron-dependent cell death pathway driven by lipid peroxidation (31,32). The data of the present study confirmed TQ/HP-β-CD induces canonical ferroptosis markers (ROS accumulation, GSH depletion and MDA elevation), positioning it alongside natural inducers such as cantharidin (33) while offering superior tumor selectivity (34). Critically, the complex outperformed aqueous TQ (TQ/H_2O) in suppressing NSCLC proliferation and migration due to enhanced intracellular delivery. It was noted that HP-β-CD alone exhibited negligible cytotoxicity and TQ/H_2O also displayed very weak cytotoxic effects due to the inherently poor water solubility of TQ. In light of this, a direct comparison of the cytotoxic differences between TQ/H_2O and HP-β-CD may not yield significant insights relevant to the primary objective of the present study, concerning the efficacy of the complex and thus such a comparison was not performed.

A key mechanistic breakthrough is the demonstration that TQ/HP-β-CD induces ferroptosis via NF-κB inhibition. While NF-κB regulates tumor survival/proliferation (35) and modulates ferroptosis (36) and TQ is known to suppress NF-κB (37), the present study was the first to link this pathway to TQ-induced ferroptosis. Ferroptotic cell death (evidenced by ROS, lipid peroxidation and GSH/MDA dysregulation) was consistently triggered in NSCLC cells and rescued by ferroptosis inhibitors. Crucially, TQ/HP-β-CD suppressed NF-κB DNA binding, while NF-κB activation reversed ferroptosis-establishing NF-κB inactivation as a critical mediator of iron-dependent oxidative damage. This expands TQ's known anticancer mechanisms beyond apoptosis (10) or PI3K/AKT modulation (11). Compared with other CDs [for example, TQ/SBE-β-CD (27)], TQ/HP-β-CD demonstrated superior translational potential, evidenced by robust *in vivo* tumor suppression (67.9% inhibition) and minimal toxicity. Its efficacy surpassed conventional chemotherapeutics including cisplatin, which induce severe side effects via apoptosis. While the present study aligned ferroptosis induction with NSCLC vulnerability, limitations remain: the molecular link between NF-κB suppression and ferroptosis execution (for example, GPX4/SLC7A11 regulation) warrants deeper investigation. Future studies should explore active targeting strategies (for example, ligand-modified HP-β-CD) to enhance tumor selectivity and evaluate synergy with immune checkpoint inhibitors.

In conclusion, TQ/HP-β-CD represents a promising NSCLC therapeutic candidate that overcomes TQ's pharmacokinetic barriers while activating a novel NF-κB-ferroptosis axis. The present study validated cyclodextrin complexation for amplifying natural compounds' therapeutic potential and positions ferroptosis induction as a compelling anticancer strategy.

Acknowledgements

Not applicable.

Funding

The present study was supported by the Guangdong Basic and Applied Basic Research Foundation (grant no. 2022A1515111167).

Availability of data and materials

The data generated in the present study may be requested from the corresponding author.

Authors' contributions

WWZ, JXD, YXL and LY conceived the present study and took responsibility for the quality of the data. WWZ and LY designed the study, completed the experiment, and supervised the data collection. JXD and YXL analyzed and interpreted the data. LY wrote the manuscript. All authors read and approved the final version of the manuscript. WWZ, JXD, YXL and LY confirm the authenticity of all the raw data.

Ethics approval and consent to participate

The present study was approved (approval no. 20240215001) by the ethics committee of Ma'anshan People's Hospital (Ma'anshan, China).

Patient consent for publication

Not applicable.

Competing interests

The authors declare that they have no competing interests.

References

1. Mithoowani H and Febbraro M: Non-small-cell lung cancer in 2022: A review for general practitioners in oncology. Curr Oncol 29: 1828-1839, 2022.
2. Meyer ML, Fitzgerald BG, Paz-Ares L, Cappuzzo F, Jänne PA, Peters S and Hirsch FR: New promises and challenges in the treatment of advanced non-small-cell lung cancer. Lancet 404: 803-822, 2024.
3. Banna GL, Hassan MA, Signori A, Giunta EF, Maniam A, Anpalakhan S, Acharige S, Ghose A and Addeo A: Neoadjuvant chemo-immunotherapy for early-stage non-small cell lung cancer: A systematic review and meta-analysis. JAMA Netw Open 7: e246837, 2024.
4. Chen YL, Xiong LA, Ma LF, Fang L and Zhan ZJ: Natural product-derived ferroptosis mediators. Phytochemistry 219: 114002, 2024.
5. Wang X, Izzo AA, Papapetropoulos A, Alexander SPH, Cortese-Krott M, Kendall DA, Martemyanov KA, Mauro C, Panettieri RA Jr, Patel HH, *et al*: Natural product pharmacology: The British Journal of pharmacology perspective. Br J Pharmacol 181: 3547-3555, 2024.
6. Zhang L, Liu P, Jiang Y, Fan D, He X, Zhang J, Luo B, Sui J, Luo Y, Fu X and Yang T: Exploration of novel isoxazole-fused quinone derivatives as anti-colorectal cancer agents through inhibiting STAT3 and elevating ROS level. Eur J Med Chem 272: 116448, 2024.
7. Muramoto J and Sakamoto T: Tripodal quinone-cyanine G-quadruplex ligands as novel photosensitizers on photoinduced cancer cell death. Molecules 29: 5094, 2024.
8. Dey A, Kumar EKP, Kim CH, Li Y and Park JH: Dual stimuli-responsive nanoprecursor of ascorbic acid and quinone methide disrupting redox homeostasis for cancer treatment. ACS Omega 9: 32124-32132, 2024.
9. Modarresi Chahardehi A, Ojaghi HR, Motedayyen H and Arefnezhad R: Nano-based formulations of thymoquinone are new approaches for psoriasis treatment: A literature review. Front Immunol 15: 1416842, 2024.
10. Abutayeh RF, Altah M, Mehdawi A, Al-Ataby I and Ardakani A: Chemopreventive agents from nature: A review of apigenin, rosmarinic acid, and thymoquinone. Curr Issues Mol Biol 46: 6600-6619, 2024.
11. Zhao ZX, Li S and Liu LX: Thymoquinone affects hypoxia-inducible factor-1α expression in pancreatic cancer cells via HSP90 and PI3K/AKT/mTOR pathways. World J Gastroenterol 30: 2793-2816, 2024.
12. Taiyab A, Choudhury A, Haidar S, Yousuf M, Rathi A, Koul P, Chakrabarty A, Islam A, Shamsi A and Hassan MI: Exploring MTH1 inhibitory potential of thymoquinone and baicalin for therapeutic targeting of breast cancer. Biomed Pharmacother 173: 116332, 2024.
13. Shakeel I, Haider S, Khan S, Ahmed S, Hussain A, Alajmi MF, Chakrabarty A, Afzal M and Imtaiyaz Hassan M: Thymoquinone, artemisinin, and thymol attenuate proliferation of lung cancer cells as Sphingosine kinase 1 inhibitors. Biomed Pharmacother 177: 117123, 2024.
14. Burdușel AC and Andronescu E: Lipid nanoparticles and liposomes for bone diseases treatment. Biomedicines 10: 3158, 2022.
15. Xie B, Liu Y, Li X, Yang P and He W: Solubilization techniques used for poorly water-soluble drugs. Acta Pharm Sin B 14:4683-4716, 2024.
16. Kowalska A and Szeleszczuk Ł: Cyclodextrin inclusion complexes with hydrocortisone-type corticosteroids. Pharmaceutics 16: 1544, 2024.
17. Sarabia-Vallejo Á, Caja MDM, Olives AI, Martín MA and Menéndez JC: Cyclodextrin inclusion complexes for improved drug bioavailability and activity: Synthetic and analytical aspects. Pharmaceutics 15: 2345, 2023.
18. Alqahtani MS, Kazi M, Alsenaidy MA and Ahmad MZ: Advances in oral drug delivery. Front Pharmacol 12: 618411, 2021.
19. Wu HH, Garidel P and Michaela B: HP-β-CD for the formulation of IgG and Ig-based biotherapeutics. Int J Pharm 601: 120531, 2021.
20. Shen Q, Shen Y, Jin F, Du YZ and Ying XY: Paclitaxel/hydroxypropyl-β-cyclodextrin complex-loaded liposomes for overcoming multidrug resistance in cancer chemotherapy. J Liposome Res 30: 12-20, 2020.
21. Saha ST, Abdulla N, Zininga T, Shonhai A, Wadee R and Kaur M: 2-Hydroxypropyl-β-cyclodextrin (HPβCD) as a potential therapeutic agent for breast cancer. Cancers (Basel) 15: 2828, 2023.
22. Al-Qubaisi MS, Rasedee A, Flaifel MH, Eid EEM, Hussein-Al-Ali S, Alhassan FH, Salih AM, Hussein MZ, Zainal Z, Sani D, *et al*: Characterization of thymoquinone/hydroxypropyl-β-cyclodextrin inclusion complex: Application to anti-allergy properties. Eur J Pharm Sci 133: 167-182, 2019.
23. Swingler S, Gupta A, Gibson H, Kowalczuk M, Adamus G, Heaselgrave W and Radecka I: Thymoquinone: Hydroxypropyl-β-cyclodextrin loaded bacterial cellulose for the management of wounds. Pharmaceutics 14: 2816, 2022.
24. Eid EEM, Alshehade SA, Almaiman AA, Kamran S, Lee VS and Alshawsh MA: Enhancing the anti-leukemic potential of thymoquinone/sulfobutylether-β-cyclodextrin (SBE-β-CD) inclusion complexes. Biomedicines 11: 1891, 2023.
25. Luo K and Hu W: A dual thermo/pH-sensitive hydrogel as 5-fluorouracil carrier for breast cancer treatment. Anti-cancer Drugs 36: 220-231, 2025.
26. Peng L, Liu A, Shen Y, Xu HZ, Yang SZ, Ying XZ, Liao W, Liu HX, Lin ZQ, Chen QY, *et al*: Antitumor and anti-angiogenesis effects of thymoquinone on osteosarcoma through the NF-κB pathway. Oncol Rep 29: 571-578, 2013.
27. Eid EEM, Almaiman AA, Alshehade SA, Alsalemi W, Kamran S, Suliman FO and Alshawsh MA: Characterization of thymoquinone-sulfobutylether-β-cyclodextrin inclusion complex for anti-cancer applications. Molecules 28: 4096, 2023.
28. Chen K, Yang R, Shen FQ and Zhu HL: Advances in pharmacological activities and mechanisms of glycyrrhizic acid. Curr Med Chem 27: 6219-6243, 2020.
29. Ma Y, Su Q, Yue C, Zou H, Zhu J, Zhao H, Song R and Liu Z: The effect of oxidative stress-induced autophagy by cadmium exposure in kidney, liver, and bone damage, and neurotoxicity. Int J Mol Sci 23: 13491, 2022.
30. Wu J, Wang Q, Dong X, Xu M, Yang J, Yi X, Chen B, Dong X, Wang Y, Lou X, *et al*: Biocompatible AIEgen/p-glycoprotein siRNA@reduction-sensitive paclitaxel polymeric prodrug nanoparticles for overcoming chemotherapy resistance in ovarian cancer. Theranostics 11: 3710-3724, 2021.
31. Li Y, Cai Z, Ma W, Bai L, Luo E and Lin Y: A DNA tetrahedron-based ferroptosis-suppressing nanoparticle: Superior delivery of curcumin and alleviation of diabetic osteoporosis. Bone Res 12: 14, 2024.
32. Zhang Z, Zhao Y, Wang Y, Zhao Y and Guo J: Autophagy/ferroptosis in colorectal cancer: Carcinogenic view and nanoparticle-mediated cell death regulation. Environ Res 238: 117006, 2023.
33. Zhu X, Chen X, Qiu L, Zhu J and Wang J: Norcantharidin induces ferroptosis via the suppression of NRF2/HO-1 signaling in ovarian cancer cells. Oncol Lett 24: 359, 2022.
34. Karki N, Aggarwal S, Laine RA, Greenway F and Losso JN: Cytotoxicity of juglone and thymoquinone against pancreatic cancer cells. Chem Biol Interact 327: 109142, 2020.
35. Yu H, Lin L, Zhang Z, Zhang H and Hu H: Targeting NF-κB pathway for the therapy of diseases: Mechanism and clinical study. Signal Transduct Target Ther 5: 209, 2020.
36. Chen Y, Fang ZM, Yi X, Wei X and Jiang DS: The interaction between ferroptosis and inflammatory signaling pathways. Cell Death Dis 14: 205, 2023.
37. Chen B, Dong X, Zhang JL, Sun X, Zhou L, Zhao K, Deng H and Sun Z: Natural compounds target programmed cell death (PCD) signaling mechanism to treat ulcerative colitis: A review. Front Pharmacol 15: 1333657, 2024.